



HAL
open science

Spatio-temporal discrimination of molecular, aerosol and cloud scattering and polarization using a combination of a Raman lidar, Doppler cloud radar and microwave radiometer

Dongxiang Wang, Iwona S. Stachlewska, Julien Delanoë, Dragos Ene, Xiaoquan Song, Dirk Schüttemeyer

► To cite this version:

Dongxiang Wang, Iwona S. Stachlewska, Julien Delanoë, Dragos Ene, Xiaoquan Song, et al.. Spatio-temporal discrimination of molecular, aerosol and cloud scattering and polarization using a combination of a Raman lidar, Doppler cloud radar and microwave radiometer. *Optics Express*, 2020, 28 (14), pp.20117-20134. 10.1364/OE.393625 . insu-02884288

HAL Id: insu-02884288

<https://insu.hal.science/insu-02884288>

Submitted on 29 Jun 2020

HAL is a multi-disciplinary open access archive for the deposit and dissemination of scientific research documents, whether they are published or not. The documents may come from teaching and research institutions in France or abroad, or from public or private research centers.

L'archive ouverte pluridisciplinaire **HAL**, est destinée au dépôt et à la diffusion de documents scientifiques de niveau recherche, publiés ou non, émanant des établissements d'enseignement et de recherche français ou étrangers, des laboratoires publics ou privés.



Spatio-temporal discrimination of molecular, aerosol and cloud scattering and polarization using a combination of a Raman lidar, Doppler cloud radar and microwave radiometer

DONGXIANG WANG,¹ IWONA S. STACHLEWSKA,^{1,*}  JULIEN DELANOË,² DRAGOS ENE,³  XIAOQUAN SONG,⁴ AND DIRK SCHÜTTEMEYER⁵

¹Faculty of Physics, University of Warsaw (FUW), Warsaw 00-927, Poland

²LATMOS/IPSL, UVSQ Université Paris-Saclay, Sorbonne Université, CNRS, Guyancourt 78280, France

³National Institute of R&D for Optoelectronics (INOE), Magurele-Bucharest 07712, Romania

⁴College of Information Science and Engineering, Ocean University of China (OUC), Qingdao 266100, China

⁵European Space Research and Technology Centre, European Space Agency (ESA), Noordwijk 2201, The Netherlands

*iwona.stachlewska@fuw.edu.pl

Abstract: The combined data from the ESA Mobile Raman Polarization and Water Vapor Lidar (EMORAL), the LATMOS Bistatic Doppler Cloud Radar System for Atmospheric Studies (BASTA), and the INOE Microwave Radiometer (HATPRO-G2) have been used to explore the synergy for the spatio-temporal discrimination of polarization and molecular, aerosol and cloud scattering. The threshold-based methodology is proposed to perform an aerosol-cloud typing using the three instruments. It is demonstrated for 24 hours of observations on 10 June 2019 in Rzecin, Poland. A new scheme for target classification, developed collaboratively by the FUW and the OUC, can help determine molecules, aerosol (spherical, non-spherical, fine, coarse), cloud phase (liquid, ice, supercooled droplets) and precipitation (drizzle, rain). For molecular, aerosol, and cloud discrimination, the thresholds are set on the backward scattering ratio, the linear particle depolarization ratio and the backscatter colour ratio, all calculated from lidar signals. For the cloud phase and precipitation categorization, the thresholds are set on the reflectivity and the Doppler velocity derived from cloud radar signals. For boundary layer particles, precipitation, and supercooled droplets separation, the thresholds are set on the profiles of temperature and relative humidity obtained by the microwave radiometer. The algorithm is able to perform separation even under complicated meteorological situation, as in the presented case study.

© 2020 Optical Society of America under the terms of the [OSA Open Access Publishing Agreement](#)

1. Introduction

The 24/7 ground-based remote sensing measurements of aerosol and clouds are an important source of information, as they can obtain high resolution, long-term data in well-defined areas on a continuous basis [e.g. 1–3]. Their data products are closer to target particles than satellite observations and have a better spatio-temporal resolution and accuracy [1]. Knowledge about aerosol and clouds on such a scale can help better assess their direct and indirect effects on radiation transfer and the balance of the Earth-atmosphere system [4–7]. As the effects of aerosol and clouds can differ significantly, depending on their optical thickness and altitude [5,6,8], they should be observed, if possible, at the same time, using instruments that are well suited for this purpose.

In many studies, aerosol and/or cloud properties are derived from measurements conducted with airborne sensors [e.g. 9–11] and space-borne sensors [e.g. 12–15]. Space-borne sensors can also provide a good temporal coverage. However, in this case the major challenge is to obtain information on aerosol and clouds with a high vertical resolution [e.g. 12,14]. Another drawback is that satellite sensors cannot conduct observations over the site of interest continuously. Thus, both active and passive ground-based remote sensing observations are necessary to complement airborne and satellite observations.

Doppler cloud radars provide information on cloud and precipitation particles, as well as on cloud dynamics [e.g. 16–19]. Cloud radars are active remote sensors, and they are more sensitive to large particles, compared with lidar. They are able to penetrate optically thick clouds, but fail to detect aerosol and clouds composed of small-sized particles [9,20]. Lidars are capable of measuring aerosol, and almost all cloud types, as long as they are the first encountered layer and their optical depth is low [e.g. 21–24]. Lidars are also active remote sensors, but their backscatter signal is proportional to the second moment of the particle size distribution, hence compared with cloud radars, lidar signals are sensitive to optically thin clouds [e.g. 12], Cirrus and contrails [e.g. 25], as well as supercooled water layers [e.g. 9,26], but cannot penetrate optically thick clouds, because of strong signal attenuation [e.g. 27]. Scanning microwave radiometers are passive remote sensors that can provide integrated-column measurements of integrated water vapor (IWV) and liquid water path (LWP), as well as profiles of relative humidity and temperature [28,29].

The target classification schemes can be applied either solely to the cloud radar (e.g. cloud droplets, ice, and precipitating particles) [30,31] or to lidar data (e.g. aerosol typing [32]). Combining lidar and cloud radar measurements can result in more complete information on aerosol and cloud properties, their vertical structure and occurrence [e.g. 33,34]. Microwave radiometer products can support target classification in combination with lidar/radar (e.g. [12,19]). The synergy between cloud radar, lidar, and microwave radiometers has proved effective for retrieving cloud properties such as ice/liquid water content and effective radius [10,12].

The aim of this paper is to propose a new threshold based methodology that can be used for studies of aerosol and cloud properties and types, including the cloud phase, using the synergy of lidar, cloud radar and microwave radiometer to provide better forecasting and climate models [18,35].

The paper is organized as follows. In section 2, instrumentation and typical data products are described. The methodology and the data products that are used for the molecules-aerosol-cloud classification are described in section 3. The current classification methodology is discussed in section 4. Section 5 gives details on the new thresholds proposed for the target classification. The results and their repercussions are provided for in section 6. The paper is summarized in section 7.

2. Instrumentation and derived data products

The three remote sensing instruments, the Raman-polarization lidar, the Doppler cloud radar and the microwave radiometer were installed in a close proximity on 10 June 2019 in Rzecin (52°45'N, 16°18'E, 54 m a.s.l.), Poland. The distance between them was fewer than 15 m. The instruments do not measure the same volume: the lidar footprint is the smallest, next is the cloud radar (half beam width 0.4°), and the microwave radiometer is the largest, which has an impact on retrievals. All instruments operated in a 24/7 detection mode, providing profiles covering almost the entire troposphere, whereby the spatial and temporal resolution of the profiles provided by each instrument was different. Each instrument is described below.

The ESA Mobile Raman Lidar (EMORAL) uses as a radiation source the Nd-YAG laser (SpitLight 400, InnoLas, Germany), operating at 1064 nm (112 mJ), 532 nm (103 mJ) and 355 nm (128 mJ). The laser emits all three wavelengths to the atmosphere simultaneously and collinearly,

with a repetition rate of 10 Hz and pulse lengths of 5-7 ns. The backward scattered radiation is collected with a Cassegrain telescope (primary mirror of 300 mm, adjustable field of view of 2-3.6 mrad), then separated and filtered to detect 8 channels: 3 elastic channels (1064 nm, 532 nm, and 355 nm), 3 vibrational Raman channels (for nitrogen at 387 nm, 607 nm and for water vapour at 407 nm), and 2 depolarization channels at 532 nm and 355 nm. All signals are recorded with an analogue and photon-counting mode, using the 16-bits transient recorders (TR40-160, Licel, Germany), except for 1064 nm (only analogue). The raw signal height resolution is 3.75 m and the time resolution is adjustable (from 2 s to 1 min). The full overlap height is at 400 m, the effect of overlap below this altitude is neglected, no overlap correction function is applied. The level-1 products comprise attenuated backscatter signals and the volume depolarization ratio. The level-2 products are the water vapour mixing ratio [36], the atmospheric boundary layer height [37], the range of aerosol optical properties [3,38-40], and the backward scattering ratio (this paper). The level-3 products comprise microphysical parameters [41]. The combination of the different level products obtained at different wavelengths can be used for aerosol and cloud typing in terms of particle size and shape, i.e. to assess aerosol-free molecular atmosphere, fine/coarse particles, spherical/non-spherical particles, water droplets, ice crystals or their mixtures. The profiles of the lidar-derived atmospheric properties used in this paper are obtained for a vertical resolution of 3.75 m and the time of 2 s. A lidar evaluation scheme applied for the data evaluation is compliant with the Quality Assurance recommendations of the European Aerosol Research Lidar Network (EARLINET) developed within the Aerosol, Clouds, and Trace Gases Research Infrastructure (ACTRIS), i.e. the full quality assure (QA) tests are applied (tele cover test, dark measurement, depolarization calibration, trigger delay [42]). The tools for the high quality lidar data evaluation are described in [e.g. 43,44].

The Bistatic Radar System for Atmospheric Studies (BASTA) is a semi-operational 95 GHz Doppler cloud radar, which uses the frequency-modulated continuous wave (FMCW) technique. The technique can be highly sensitive with much less power than traditional pulsed systems, there are some advantages and some disadvantages of using it [45]. It was installed next to the EMORAL lidar (circa 15 m away). It provides real time 24/7 vertical observations of the cloud structure and properties (such as cloud fraction, cloud phase, cloud water content, etc). It uses a specific signal processing technique in such a way that the radar can provide high-quality measurements of cloud and fog. The main products are reflectivity and Doppler velocity (level-1), obtained successively with 12.5 m, 25 m and 100 m vertical resolution and 3 s time resolution. The lower limit is 125 m for all modes. The 12.5 m mode is limited to 12 km. The 25 m and 100 m modes cover the range up to 18 km. A merged product is derived making the most of the sensitivity and resolution of each mode, i.e. a combination of different vertical resolutions is applied at different altitude ranges. The resulting vertical resolution of the merged product is height-dependent and it is of 12.5 m below 0.5 km, 25 m between 0.5 and 5 km, and 100 m above 5 km. The integration time is 9 s for the merged product. The level-2 products (rain, drizzle, ice cloud and liquid particles and droplets) and the level-3 products (microphysical cloud properties) can also be obtained. The three successive modes are used for specific applications: the 12.5 m vertical resolution mode is dedicated to fog and low clouds, the 25 m mode is for liquid and ice mid-tropospheric clouds, and the 100 m is ideal for optically thin, high-level ice clouds. The radar comes with a set of products dedicated to cloud and fog studies. For instance, a cloud mask, corrected Doppler velocity and multi-mode products combining a high sensitivity mode and high-resolution mode are provided. More details can be found in [10,45] and <http://basta.projet.latmos.ipsl.fr>, last access: 28 February 2020. The cloud radar has been calibrated based on the methodology given in [45,46,47], which is typically applied for high-quality data retrieval in the Cloud Observation Network (CLOUDNET) within the ACTRIS.

The microwave radiometer (HATPRO-G2, Radiometer Physics GmbH) was installed in a proximity of the BASTA cloud radar (circa 2 m away). The microwave radiometer consists of two

working bands at 22–31 and 51–58 GHz, each with seven channels [48]. The vertical resolution of this instrument is much coarser than that for the other two instruments. Measurements with a temporal resolution of 15 s and a height-dependent vertical resolution: 200 m from 0 to 2 km, 400 m from 2 to 5 km, and > 500 m for the heights above 5 km [49]. The level-1 products are brightness temperatures. The level-2 products are integrated water vapour (IWV), liquid water path (LWP), and the vertical profiles of absolute humidity (AH), relative humidity (RH), water vapor (WV), temperature (T) and boundary layer height (ABL). The profiles of temperature and water vapour are calculated from the brightness temperatures using statistical regression algorithms [50]. To ensure high quality of the observation, the absolute calibration is done using liquid nitrogen, according to the details in [51]. The data quality control was done compliant with the methodology described in [48].

3. Methodology

Different optical properties of aerosol and cloud can be obtained from lidar signals [e.g. 22,24,52]. The backscatter signal P can be described with the classical elastic lidar equation:

$$P = C \frac{O}{R^2} (\beta_p + \beta_m) \exp \left\{ -2 \int_0^R (\alpha_p + \alpha_m) dr \right\} \quad (1)$$

where C is the instrumental constant (system factor), R is the range of the lidar signal, O is the overlap function that equals 1 at the complete overlap between the laser beam and the full field of view of the telescope, β_p is the particle backscatter coefficient, β_m is the molecular backscatter coefficient, α_p is the particle extinction coefficient, α_m is the molecular extinction coefficient.

When the lidar system is equipped with the Raman channels, the extinction coefficient profiles can be derived using the Raman method. It has its limitations related to a relatively weak Raman scattering cross-section at the detected wavelength in comparison to the elastic scattering cross-section at the initial wavelength. This matters especially if the Raman method is applied during the daytime. Sunlight radiation affects the signal to noise ratio, which can be improved at the cost of reducing temporal and spatial resolutions. This limits the retrieval to 2 km in the daytime for a 30-minute averaged profile and 120 m height resolution. At night, profiles reach 3.5 km for the same averaging. Hence, the Raman method was considered as not sufficiently consistent in terms of quality and performance to provide products for use in the 24/7 classification scheme. Therefore, the Klett-Fernald method was chosen [53,54].

The particle backscatter (β_p) and extinction (α_p) coefficient profiles in the Klett-Fernald method are obtained using elastic lidar signals [Eq. (1)] by solving the Bernoulli differential equation with the assumption of the height independent particle lidar ratio ($LR_p = \alpha_p / \beta_p$), calibrated at a certain height-range of the atmosphere, where only molecular scattering occurs [53,54]. There is an obvious difficulty to choose the appropriate lidar ratio and the calibration range in the presence of low-level clouds or when aerosol load is high. Therefore, the attenuated backscatter coefficient (β_a) is often used instead, as described in [24], defined in Eq. (2):

$$\beta_a = \frac{PR^2}{C} \quad (2)$$

The C can be calculated as in Eq. (3):

$$C = \frac{PR^2}{(\beta_p + \beta_m) O} \exp \left\{ 2 \int_0^R (\alpha_p + \alpha_m) dr \right\} \quad (3)$$

The C is generally stable in a daytime scale [24], thus it can be calculated once per day for the clear sky observation period. If there is no clear sky on the observational day, the C can be calculated for adjacent days with a clear sky period. The β_p profiles used for the C calculation

can be computed with the aforementioned approach [53,54] and the β_m can be calculated using the atmospheric profiles of the 1976 US standard atmosphere (note that rawinsondes can be used, if available close to the observational site). The particle lidar ratio (LR_p) of 55 sr can be used as a reference, as such it is applied at several European continental sites for long-term statistical studies [e.g. 3]. The final system factor C is calculated as the mean value of the height between 1 and 2 km in Eq. (3).

The determination of the quasi-particle backscatter coefficient ($^{quasi}\beta_p$) is in accordance with to the reference [24], i.e. it is done as a 2-step process, where the Eq. (4) gives the first guess of $^{quasi*}\beta_p$ (indicated with *) that is used to obtain the quasi-particle extinction coefficient ($^{quasi}\alpha_p$), as in the Eq. (5). Then the Eq. (6) is used to calculate the final quasi-particle backscatter coefficient value.

$$^{quasi*}\beta_p = \beta_a \exp \left\{ 2 \int_0^R \alpha_m dr \right\} - \beta_m \quad (4)$$

$$^{quasi}\alpha_p = ^{quasi*}\beta_p LR_p \quad (5)$$

$$\beta_p \approx ^{quasi}\beta_p = \beta_a \exp \left\{ 2 \int_0^R (^{quasi}\alpha_p + \alpha_m) dr \right\} - \beta_m \quad (6)$$

The linear volume depolarization ratio (δ_v) can be derived from the lidar data as the ratio of the backscatter signal from the vertically-polarized signal channel (P_v) and the corresponding parallel-polarized signal channel (P_p), as in Eq. (7).

The linear particle depolarization ratio (δ_p) is nearly equal to the linear quasi-particle depolarization ratio ($^{quasi}\delta_p$), derived as in Eq. (8). Note that the β_p is replaced by the $^{quasi}\beta_p$ (defined as in Eq. (6)) for this calculation:

$$\delta_v = \frac{P_v}{P_p} \quad (7)$$

$$\delta_p \approx ^{quasi}\delta_p = \frac{(1 + \delta_m)\delta_v \left(1 + \frac{^{quasi}\beta_p}{\beta_m} \right) - (1 + \delta_v)\delta_m}{(1 + \delta_m) \left(1 + \frac{^{quasi}\beta_p}{\beta_m} \right) - (1 + \delta_v)} \quad (8)$$

where δ_v is the linear volume depolarization ratio, δ_m is the linear depolarization ratio of air molecules. The δ_v and δ_p quantities in Eqs. (7) and (8), are obtained using the $\Delta 90$ depolarization calibration [55,56]. These quantities proved to be very useful to distinguish between spherical (low depolarization ratios) and non-spherical particles (high depolarization ratios) [e.g. 57,58].

The properties of cloud and precipitation can be obtained from the Doppler cloud radar [e.g. 10,16]. The cloud radar target classification (rain, drizzle, ice cloud and liquid) is retrieved from the level-1 products (i.e. the reflectivity and the Doppler velocity). In a first approximation, assuming small particles and therefore in Rayleigh regime, the reflectivity (Z) can be represented as in Eq. (9) for the number of reflective particle diameters $N(D)$ and the size of reflective particles D .

$$Z = \int_0^{\infty} N(D) D^6 dD \quad (9)$$

When it comes to the microwave radiometer (MWR), temperature profiles can be used to provide an important reference for the separation of aerosol layers (e.g. supercool layer, liquid cloud) and cloud types (liquid, ice or mixed phase). The relative humidity can be used as an important reference for separation of a dry and wet environment.

4. Current classification methodology

An atmospheric constituent/target classification is, in general, a challenging task. It has been developed by several groups [e.g. 9,12,24,32], using different techniques and methods applied for the separation of different targets throughout the atmosphere. The majority of developments in this field were done in relation to satellite observations with Cloud-Aerosol Lidar and Infrared Pathfinder Satellite Observations CALIPSO (National Aeronautics and Space Administration, NASA, USA, and National Centre for Space Studies, CNES, France) and CloudSat (NASA). A methodology for the classification of aerosol, rain, liquid, supercooled and ice clouds using datasets from the Cloud Profiling Radar onboard CloudSat and the Cloud-Aerosol Lidar with Orthogonal Polarization (CALIOP) onboard CALIPSO, collocated in time and space is extensively discussed in [9]. Categorization of molecular, aerosol, rain, supercooled and ice clouds using the A-Train satellite constellation data – spaceborne lidar, radar and infrared radiometers was proposed by [12]. Another scheme for classification of ice cloud, mixed-phase cloud, and supercooled layers in Arctic region using airborne cloud radar and lidar data is discussed in [23]. In the study of [23], the lidar was mainly used for identifying supercooled layers, while in [12] the lidar was also used to separate molecular and aerosol in addition to identifying the supercooled layers. In none of these papers a further classification with regards to the aerosol type nor the aerosol shape was attempted. Categorizations of aerosol and cloud types using the thresholds on the ground-based lidar, but with no rain/drizzle and thick clouds typing due to the usage of a single instrument was proposed by [24].

In existing studies, atmosphere was classified using thresholds on the lidar products, such as: particle backscatter coefficient [e.g. 22,24], and/or particle depolarization ratio [e.g. 24,59], and/or Ångström exponent [e.g. 24,60]. The different thresholds are described below.

The particle backscatter coefficient (β_p) was used to discriminate molecular, aerosol, and cloud scattering based on space-borne [e.g. 22,61] and ground-based observations [24]. For aerosol and clouds classification of CALIPSO lidar, the study in [61] considered clear-sky atmosphere for $\beta_p(1064 \text{ nm}) < 1 \times 10^{-8} \text{ m}^{-1} \text{ sr}^{-1}$, clouds for $\beta_p(1064 \text{ nm}) > 2 \times 10^{-5} \text{ m}^{-1} \text{ sr}^{-1}$, and aerosol for values in between. For the CALIPSO lidar in the study of [59], a threshold of $\beta_p(1064 \text{ nm}) > 1 \times 10^{-5} \text{ m}^{-1} \text{ sr}^{-1}$ was used for discrimination of clouds from aerosol. In the study of [24], for *quasi* $\beta_p(1064 \text{ nm}) > 2 \times 10^{-7} \text{ m}^{-1} \text{ sr}^{-1}$ ice clouds were separated from aerosol for the ground-based lidar. The latter threshold was considered as an equivalent to the one used in the CALIPSO feature mask, i.e. the attenuated backscatter $\beta_a(532 \text{ nm}) > 5 \times 10^{-7} \text{ m}^{-1} \text{ sr}^{-1}$ separating ice clouds from aerosol [22].

The particle depolarization ratio (δ_p) was used to discriminate spherical and non-spherical particles [22,24]. The particle was regarded as non-spherical with the $\delta_p(532 \text{ nm}) > 0.2$ and as spherical when $\delta_p(532 \text{ nm}) < 0.05$ [22]. Particles were considered as non-spherical for the quasi-particle depolarization ratio *quasi* $\delta_p(532 \text{ nm}) > 0.2$ and spherical for *quasi* $\delta_p(532 \text{ nm}) < 0.07$ and a mixture for values in between [24].

The Ångström exponent (ÅE) was used to discriminate aerosol particles size and aerosol type [e.g. 24]. The ÅE can be calculated using e.g. particle extinction coefficients, particle backscatter coefficients, aerosol optical depths (the obtained values are not directly comparable). The threshold of $\text{ÅE}(532/1064 \text{ nm}) \geq 0.75$ was used for separating small particles from the large ones in the aerosol classification scheme [24].

In the current paper, other quantities are proposed to be used for classification, namely the scattering ratio (SR) to separate molecular, aerosol and cloud scattering regions and the backscatter colour ratio (CR) to discriminate an aerosol particle size. This is the first algorithm that uses thresholds on lidar-derived SR and CR products to be applied in the classification scheme based on the lidar, cloud radar, and microwave radiometer.

5. Improved target classification

A new classification scheme is proposed. It can be currently considered as the most advanced in terms of discrimination of molecular, aerosol, and cloud scattering and polarization properties. The proposed categorization relies on physical features (e.g. scattering properties, depolarizing properties, particle size) and it is based on a literature review and a sensitivity study on how the change in the threshold affects the consistency of the results. Currently, there are no operational algorithms that use the proposed combination of instruments, whereby this combination has some significant advantages. Target classification workflow based on SR , $^{quasi}\delta_p$, CR , Z , V , T and RH profiles is illustrated in Fig. 1. The data product profiles from the cloud radar (12.5, 25, and 100 m vertical and 9 s time resolutions), the microwave radiometer (200, 400, 500 m of vertical and 15 s time resolutions) are the lidar (30 m vertical and 30 s time resolutions) are combined to ensure that all observe a similar column of the atmosphere. Many classification schemes prefer not to use threshold values on their own, unless the threshold value provides a clear separation between two classes [e.g. 9,22,24]. This is also in our case.

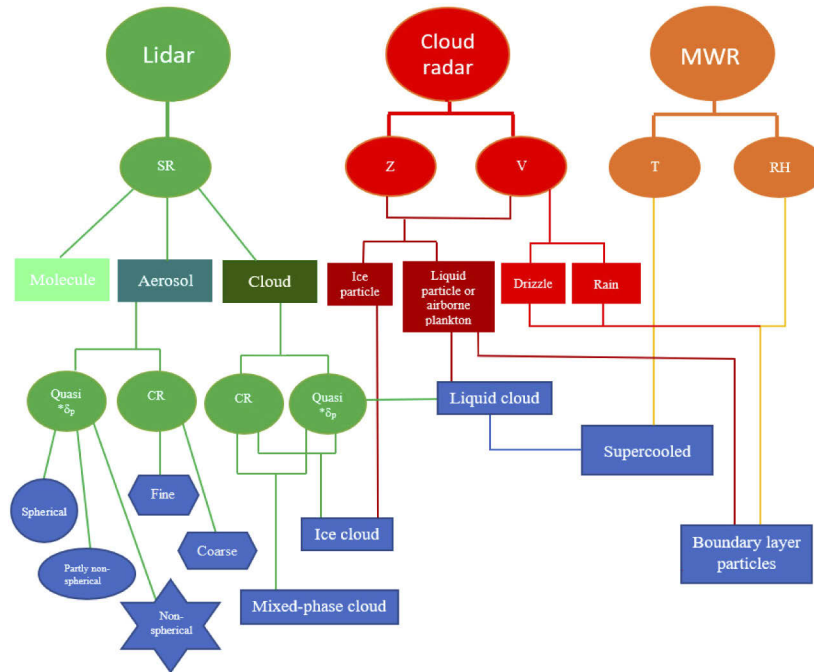


Fig. 1. The flowchart of the target classification procedure using the combination of data from the Raman-polarization lidar, Doppler cloud radar, and microwave radiometer (MWR).

5.1. Target classification of lidar with new threshold types

A new method, based on the thresholds on the scattering ratio (SR), is applied in this study, whereby the SR is defined as the ratio of the quasi-total backscatter coefficient ($^{quasi}\beta$) and the molecular backscatter coefficient (β_m), as Eq. (10):

$$SR = \frac{^{quasi}\beta}{\beta_m} = \frac{(^{quasi}\beta_p + \beta_m)}{\beta_m} \tag{10}$$

The SR of 1 represents no scattering on aerosol particles in the atmosphere. The SR (532 nm) values for tropospheric aerosol are within the range of 1.2–1.33 over North India and Western

China, obtained based on the CALIOP lidar [62]. Over the United States of America, the SR (532 nm) of dust and smoke in the troposphere is of 2.3 and 2.9, based on the NASA Langley airborne High Spectral Resolution Lidar (HSRL) measurements [63]. The SR (532 nm) of volcanic ash aerosol ranges from 1.1 to 3.5 using lidar observations in Russia [64]. The SR (532 nm) of aerosol under dust conditions is distributed between 3 and 9 in the central Himalayas [65]. The SR (532 nm) > 5 was observed by [66] using airborne lidar when the mineral dust appeared in the Arctic. In most cases reported in literature, the threshold of the lidar derived SR at 532 nm used for the separation of molecule from aerosol is within 1.1-1.3. In this study, we set the SR (532 nm) $< 1.4 \pm 9\%$ for molecule. The SR (532 nm) > 10 was considered as cloud [66], thus we set the SR (532 nm) $> 10 \pm 20\%$ to discriminate clouds. The values between the two thresholds denote aerosol (Table 1).

Table 1. The new classification thresholds applied on the backscatter scattering ratio (SR), quasi-particle depolarization ratio ($^{quasi}\delta_p$), and backscatter colour ratio (CR) used for molecules, aerosol and cloud typing based on lidar observations.

Raman-polarization lidar measurements			
	New method	Standard method	New method
	Scattering ratio (SR)	Quasi-particle depolarization ratio ($^{quasi}\delta_p$)	Colour ratio (CR)
Molecules	$SR < 1.4 \pm 9\%$	-	-
Aerosol	$1.4 \pm 9\% \leq SR < 10 \pm 20\%$		
fine			$CR > 2.5 \pm 5\%$
coarse			$CR < 1.6 \pm 5\%$
spherical		$^{quasi}\delta_p < 0.08 \pm 13\%$	
non-spherical		$^{quasi}\delta_p \geq 0.18 \pm 11\%$	
partly non-spherical		$0.08 \pm 13\% \leq ^{quasi}\delta_p < 0.18 \pm 11\%$	$1.6 \pm 5\% \leq CR \leq 2.5 \pm 5\%$
Cloud	$SR \geq 10 \pm 20\%$		
liquid		$^{quasi}\delta_p < 0.10 \pm 13\%$	-
ice		$^{quasi}\delta_p \geq 0.35 \pm 11\%$	$CR < 0.5 \pm 5\%$
mixed-phase		$0.10 \pm 13\% \leq ^{quasi}\delta_p < 0.35 \pm 11\%$	$CR < 1 \pm 5\%$

The sensitivity constitutes a reference for the selected threshold. Taking $SR < 1.4 \pm 9\%$ as an example, means that SR within 1.3-1.5 can be used as a threshold for separating molecules and aerosol. The % denotes the actual sensitivity range, in this example, the threshold was fixed initially at 1.4 and a solution (categorization) was obtained. The sensitivity of the solution was assessed by introducing a small change, applied in an iterative way. The new result (obtained after the change was introduced) was compared with the initial solution. If the profiles (categories) were not significantly different ($< 5\%$), further change was introduced. When the initial and changed profiles differed above this limit, it was considered an actual limit (listed in the Table 1). In this example, introduction of $\pm 9\%$ change of the initial threshold value brought no significant change in the derived classification. Thus the sensitivity relating to all thresholds applied on lidar products established uncertainty in terms of %. Sensitivity related to instruments is not discussed.

A new methodology, based on the thresholds on the backscatter colour ratio (CR), is applied in this study, whereby the CR , which is related to aerosol size, is defined as the ratio of the quasi particle backscatter coefficient at 532 nm and 1064 nm, as Eq. (11):

$$CR(532/1064) = \frac{^{quasi}\beta_{p532}}{^{quasi}\beta_{p1064}} \quad (11)$$

The reported range of CR (532/1064) was 1.7-3 for pollution, 0.5-1.5 for pure dust, 1.16-1.96 for mixed dust, > 2.6 for smoke, and < 1.7 for marine particle, based on airborne HSRL observations over four field sites in Europe and Africa [67]. The range of CR (532/1064) for anthropogenic pollution 1.5-2.5, pure dust 0.5-1.5, mixed dust 1.0-2.0, smoke 1.8-2.8, and marine particle 1.2-1.6 were reported based on airborne HSRL observations over North America from 2006 until 2010 [60]. Moreover, the mean value of CR (532/1064) was determined, for pollution it was 1.8 ± 0.1 , for dust 0.70 ± 0.07 , for smoke 1.7 ± 0.1 , and for marine 1.1 ± 0.1 [68]. In literature, values of CR (532/1064) > 2.6 are typically associated with fine particles (pollution, smoke) and CR (532/1064) < 1.6 with coarse particles (dust, marine particle). The CR (532/1064) < 0.8 is reported for ice particles [69]. In order to make a more precise classification on fine and coarse particles, in the current study, fine particles are considered for CR (532/1064) $> 2.5 \pm 5\%$, while coarse particles for CR (532/1064) $< 1.6 \pm 5\%$. In addition, ice particles are considered for CR (532/1064) $< 0.5 \pm 5\%$ (Table 1).

The low values of δ_p (532) < 0.01 were considered as due to very small spherical particles (e.g. [70,71]), values between 0.04-0.1 as spherical particles [72,73], 0.2-0.35 as non-spherical particles (e.g. [72]). A mixture of non-spherical and spherical particles was considered for between $0.07 < \delta_p$ (532 nm) < 0.2 , while above 0.2 the particles are categorized as large and non-spherical [58,74]. In most cases reported in literature, lidar derived δ_p (532 nm) is < 0.1 for spherical particles (e.g. smoke, marine, pollution) and δ_p (532 nm) > 0.2 for non-spherical particles (e.g. dust, ice particles). The values in between are seen for partly non-spherical particles (e.g. small pollen grains, mixture of anthropogenic pollution with dust and/or biomass burning smoke). In order to make a more precise classification on spherical and non-spherical particles, in the current study, aerosol particles characterized by $quasi \delta_p$ (532 nm) $> 0.18 \pm 11\%$ are regarded as non-spherical particles and $quasi \delta_p$ (532 nm) $< 0.08 \pm 13\%$ as spherical ones, and partly non-spherical in between (Table 1).

The new threshold types/values used for the separation of molecule, aerosol and cloud spatio-temporal ranges from the lidar observations are listed in Table 1. The SR was used for identifying and discriminating molecule, aerosol and clouds. The shape of an aerosol particle was classified by $quasi \delta_p$ that consist of spherical, partly non-spherical and non-spherical particles discrimination. The particle size was assessed based on the CR . An example of the profiling in terms of these properties is shown in Fig. 2.

5.2. Target classification of cloud radar

The target classification of the cloud radar is based on the existing scheme [e.g. 9,10,12,45] and consists of the following five classes: ice particle, liquid particle or airborne plankton (during summer), drizzle, rain, and no cloud. The liquid area (liquid cloud, drizzle and rain) is defined by the threshold on the Doppler velocity and reflectivity, as in [12,75]. The typical thresholds, as in other studies, were used for the radar-alone classification scheme, which are listed in Table 2. One can also identify melting layers, e.g. by searching in the Doppler velocity for the altitude where particles start to fall [9] or in the reflectivity for the step-wise increase at the altitude where ice particles start to get coated in liquid water [10]. In our study, the melting layer is defined as below 6 km, for the Doppler velocity gradient $dV/dr \geq 0.021s^{-1}$ and reflectivity gradient $dZ/dr \leq 0.025$ dBz $^{-1}$. An example of the profiling in terms of these properties is shown in Fig. 3.

5.3. Target classification of the microwave radiometer with new threshold types

The microwave radiometer data proved to be useful in the target classification based on space-borne [e.g. 12], airborne [e.g. 9] and ground-based measurements [e.g. 18]. The profiles of temperature (T) indicate warm ($> 0^\circ C$) and cold areas ($< 0^\circ C$) throughout the troposphere. Liquid, ice and mixed-phase clouds can be detected by the lidar. The liquid cloud layer can contain warm liquid water or supercooled water particles. The lidar alone is not able to discriminate

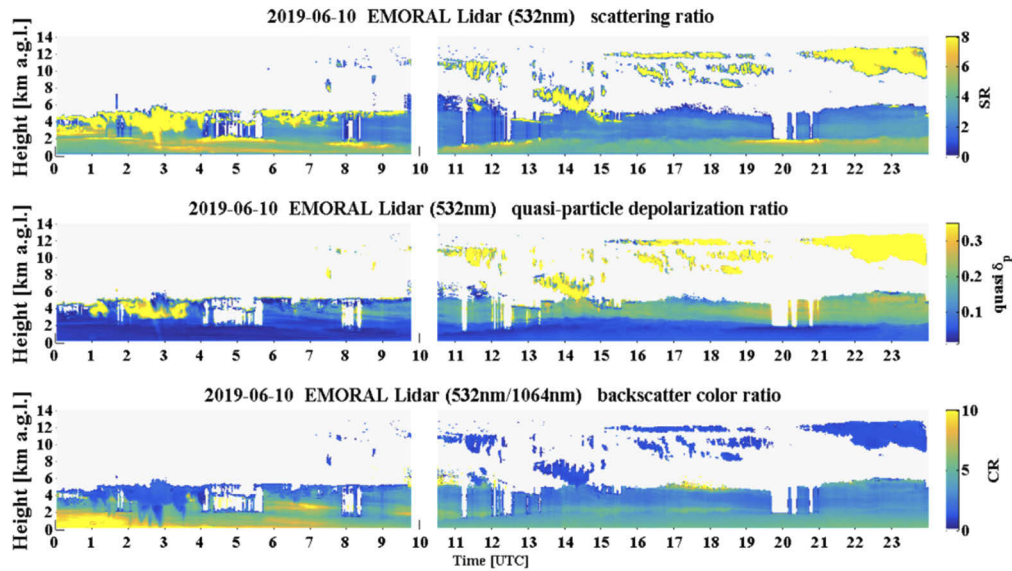


Fig. 2. The EMORAL lidar observations at the PolWET site in Rzecin, Poland, on 10 June 2019. The scattering ratio (top), quasi-particle depolarization ratio (middle), and backscatter colour ratio (bottom) derived at 532 nm with 30 m spatial and 30 s temporal resolutions.

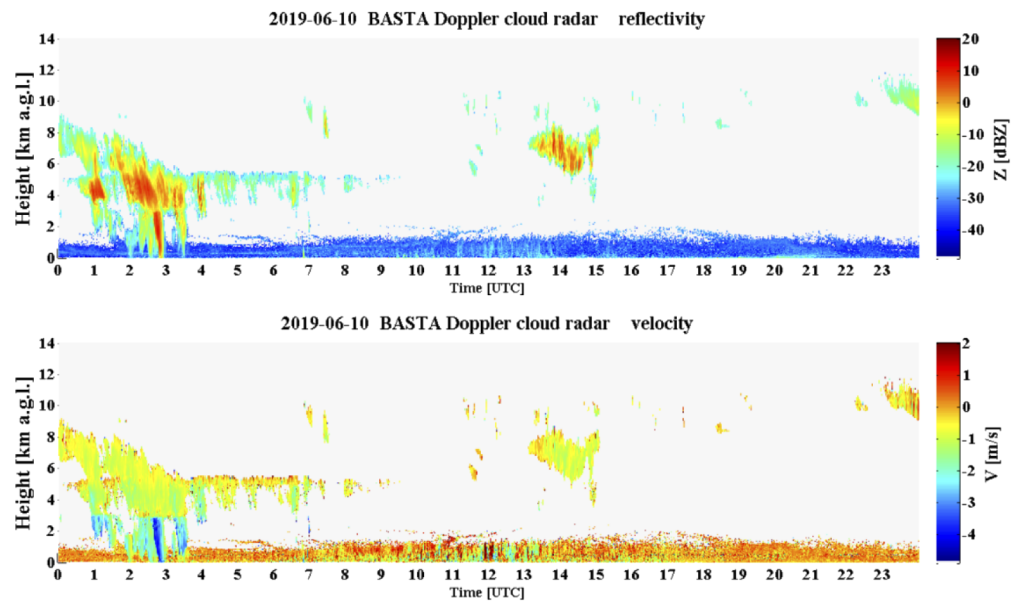


Fig. 3. BASTA cloud radar observations at the PolWET site in Rzecin on 10 June 2019. The reflectivity (top) and Doppler velocity (bottom) at merged vertical resolution (12.5, 25 and 100 m) and 9 s time integration.

Table 2. Target classification applied on reflectivity (Z) and Doppler velocity (V) using cloud radar.

Doppler cloud radar measurements		
	Standard method	Standard method
	Doppler velocity (V)	Reflectivity (Z)
Ice particle	$V \geq -0.5$ m/s	-
Liquid particle or airborne plankton	$V \geq -0.5$ m/s	$Z < 17$ dBz
Drizzle	$-1.5 < V < -0.5$ m/s	-
Rain	$V \leq -1.5$ m/s	-

between them. Therefore, temperature profiles are needed and serve as an important parameter for judging the probability of existence of supercooled particles layers [e.g. 19]. The liquid water clouds with the temperature between -40 °C and 0 °C measured by microwave radiometer are regarded as supercooled layers.

In the boundary layer, the precipitation particles/droplets and other very large-size scatter targets (airborne plankton in summer) can be separated using a combination of the cloud radar (rain/drizzle) and the microwave radiometer relative humidity (RH). The RH values indicate wetter ($\geq 65\%$) and drier areas ($< 65\%$) in the atmosphere. Rain and drizzle detected at first by the cloud radar is confirmed with the threshold on $RH \geq 65\%$. When $RH < 65\%$, the rain/drizzle detected by the cloud radar within the boundary layer is defined as unknown boundary layer particles. The thresholds used are listed in Table 3. An example of the profiling in terms of these properties is shown in Fig. 4.

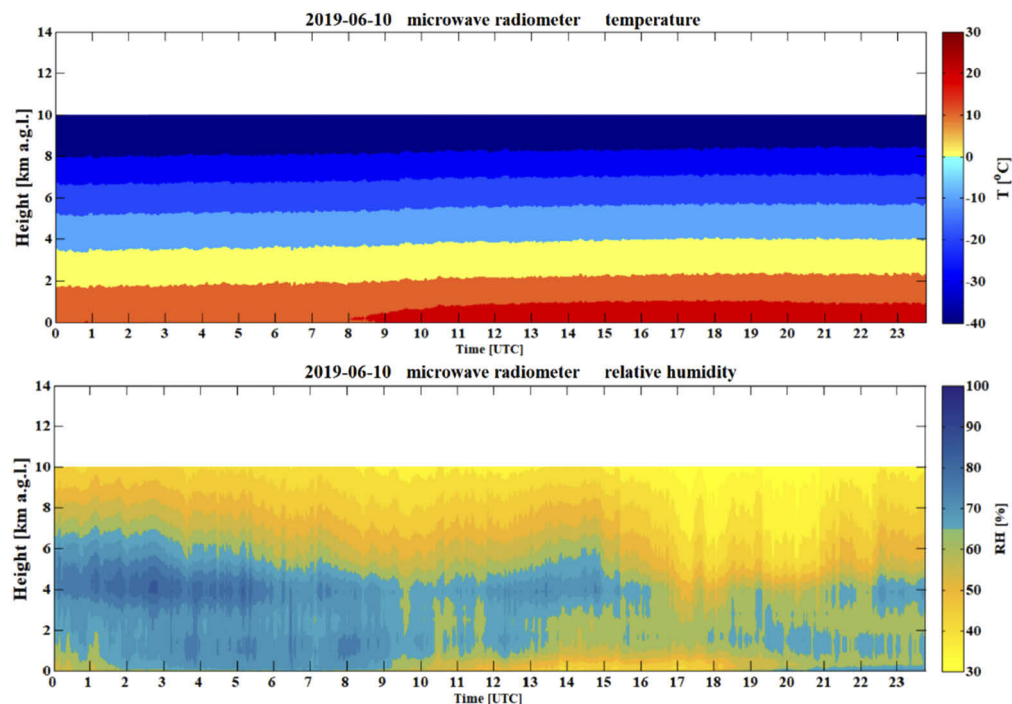


Fig. 4. The profiles of temperature (T) and relative humidity (RH) obtained from HATPRO-G2 microwave radiometer at the PolWET site in Rzecin on 10 June 2019.

Table 3. Target classification applied on temperature (T) and relative humidity (RH) using microwave radiometer (MWR).

Microwave radiometer measurements		
	Standard method	New method
	Temperature (<i>T</i>)	Relative humidity (<i>RH</i>)
Supercooled	Liquid cloud & $-40^{\circ}\text{C} < T < 0^{\circ}\text{C}$	-
Ice particle	Ice or Liquid cloud & $T \leq -40^{\circ}\text{C}$	-
Rain/drizzle in boundary layer	-	precipitation & $\text{RH} \geq 65\%$
Unknown particles in boundary layer	-	precipitation & $\text{RH} < 65\%$

6. Results and discussions

The measurements used in this paper were obtained during a joint field campaign as part of two European Space Agency (ESA) activities: The Technical Assistance for the Polish Radar and Lidar Mobile Observation System (POLIMOS) and the Technical Assistance for a Romanian Atmospheric Mobile Observation System (RAMOS).

The proposed methodology is demonstrated in a case study for 24 h observations conducted with the Raman-polarization lidar, Doppler cloud radar and microwave radiometer on 10 June 2019. On that day, characterized by different aerosol and cloud types and precipitation over the site, the fine quality of the proposed method can clearly be demonstrated.

The lidar-derived SR , $quasi\delta_p$ and CR at 532 nm and the cloud radar Z and V on 10 June 2019 are shown in Figs. 2 and 3, respectively.

Microphysical characteristics (size and shape) of the particles lead to clearly seen differences in lidar and radar observations. At the lidar wavelength of 532 nm, cloud particles scatter in the geometric optics regime, where the backscattered intensity is proportional to the square of the particle diameter (D^2), and consequently dominated by liquid droplets, due to their large number concentration [75]. On the other hand, radar reflectivity is, in the Rayleigh regime approximation, proportional to a much higher moment (D^6), and hence, it is dominated by ice particles, because of their large diameter [12].

The day started with a stratocumulus cloud with the base at around 4.5 km (captured by the lidar) and the top at around 9 km (captured by the cloud radar). Note that the altitude marking the top of the cloud shows a slow declining trend for 9 to 5 km until 04:00 UTC. The Doppler velocity shows negative values between 01:00 and 04:00 UTC, which indicates precipitation during this period. The lidar derives the cloud base well, but it cannot penetrate deeply into the thick cloud, while the radar can, and thus, it is able to detect its top. Using a combination of both is a good way to obtain the base and the top of liquid, mixed-phase and thick ice clouds.

For optically thin ice-clouds, this combination is not always available, as the radar has difficulty detecting them. Thus, above 10 km, optically thin Cirrus was observed mainly by the lidar, which is manifested also by high (for ice-clouds) $quasi\delta_p > 0.35$. Cirrus was detected by the radar only occasionally, which confirms their low optical thickness. The temperature above 6 km is below -30°C , which shows that Cirrus is mainly composed of ice crystals.

A supercooled layer from 12:30 to 13:30 UTC at the altitude of 4.8 km is likely to be found where lidar echo is strong (Fig. 2) but no radar echo was detected (Fig. 3). The profiles of temperature and relative humidity obtained by the microwave radiometer (Fig. 4) show the 0°C line at the height of 3.5 km this day. Below 0°C , there is a cold area where supercooled droplets and ice particles are likely to exist. Above 0°C , there is a warm area where liquid particles are likely to exist.

Figure 5 shows the new combined target classification created by the synergy of the lidar, cloud radar and microwave radiometer utilizing all thresholds. The categorization of molecule,

aerosol (spherical, partly non-spherical, and non-spherical, fine, and coarse) and cloud (liquid and ice) according to the new thresholds of SR , $quasi\delta_p$, and CR (Table 1) was derived for the lidar. Rain, drizzle and ice and liquid particles, relying on the threshold of Z and V (Table 2), were classified using the cloud radar.

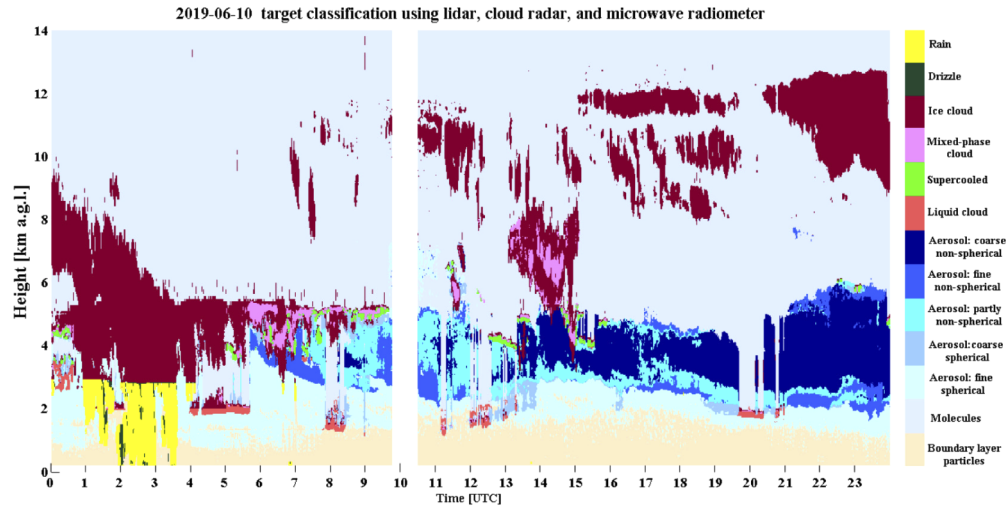


Fig. 5. Synergy for molecule, aerosol and cloud identification derived from a combination of EMORAL Raman-polarization lidar, BASTA Doppler cloud radar, and HATPRO-G2 microwave radiometer over the PolWET site in Rzecin on 10 June 2019.

On 10 June 2019, from 06:00 to 13:00 UTC, the mixed aerosol layer with spherical and non-spherical particles is observed at 2-6 km by the lidar (cyan colour in Fig. 5), then from 13:00 to 24:00 UTC as a thin layer at 2 km. The aerosol directly above it, at 3-6 km has non-spherical particles visible (dark blue in Fig. 5). The backward trajectories, calculated using the Hybrid Single-Particle Lagrangian Integrated Trajectory (HYSPLIT) model with the Global Data Assimilation System (GDAS) and CDC1 meteorological reanalyses, indicated a dust transport from the Sahara region towards the observational site at that time/height (not shown for the sake of brevity).

The rain (yellow colour in Fig. 5) and drizzle (dark green in Fig. 5) appeared with a connection to the ice cloud (dark red in Fig. 5) between 01:00 and 04:00 UTC. Between 10:30 and 20:30 UTC, the radar indicated some rain and drizzle at the height below 2.2 km, but the relative humidity (RH) was below 65% (dry environment) at this part of the day. There was also no signature of liquid clouds in lidar data directly above the radar derived rain/drizzle. That means that undefined large particles (detected by the radar but too sparse for lidar) existed inside the atmospheric boundary layer (beige colour in Fig. 5). Note that the class called boundary layer particles corresponds to the areas where cloud radar detect liquid cloud or airborne plankton and the lidar does not detect any liquid layer. The airborne plankton (pollens or insects) is made of particles too sparsely present in the air and often also too large to be detected with the lidar but large enough to be detected by the radar. Before that, between 6:00 and 9:00 UTC, the RH was $> 65\%$, so they are categorized as drizzle or rain below 2.2 km (yellow, green in Fig. 5).

The change in the Doppler velocity (in Fig. 3) at around 3 km altitude from 01:00 to 3:30 UTC (dark red and yellow/dark green in Fig. 5) indicates the existence of a melting layer, where ice crystals melt into raindrops, which constitutes a cold rain system (originating in ice).

Liquid cloud layers (light red in Fig. 5) and a mixed cloud phase (pink in Fig. 5) are observed below 5 km, while ice clouds are mainly distributed above 5 km (dark red colour in Fig. 5).

Strong backscatter regions in the lidar are composed either of warm liquid water, supercooled water (light green in Fig. 5), ice in high concentration (dark red), or a mixture of them (pink).

Locating supercooled water layers is crucial, as they represent a major weather hazard in aeronautics and can cause fatalities [76] and radiative transfer calculations [77]. The method to identify supercooled water layers was described before [e.g. 9,12,19]. Supercooled layers are usually physically thin (no more than 300 m) and observed in regions, where the temperature is between $-40 < T < 0^{\circ}\text{C}$ [12,19]. Note that supercooled or liquid clouds have the same signature in lidar signals if there is no drizzle below them. According to the temperature plots in Fig. 4, (a) cold area ($T < 0^{\circ}\text{C}$, ice or supercooled layers) is above 3.5 km. Therefore, several supercooled droplets mixed with ice particles are detected above 4 km this day (light green in Fig. 5). In addition, the values of liquid water path (not shown for the sake of brevity) between 00:00 and 07:00 UTC were clearly higher than values between 08:00 and 24:00 UTC, which can be explained by rain and a liquid cloud between 00:00 and 07:00 UTC.

7. Conclusion

A target classification based on the case study of 10 June 2019 in Rzecin, Poland, conducted using a combination of the EMORAL Raman lidar, BASTA Doppler cloud radar, and HATPRO-G2 microwave radiometer was presented. The thresholds on the particle backward scattering ratio and the linear particle depolarization ratio calculated from lidar signals are used for the separation of molecular, aerosol, and cloud signatures. Apart from that, the colour ratio computed from lidar-derived particle backscatter coefficients is utilized to discern aerosol size. The thresholds on Doppler velocity and reflectivity of the cloud radar are used for categorizing drizzle, rain, ice and liquid particles. Supercooled droplets are estimated using temperature profiles from the microwave radiometer and relative humidity profiles are used for separating rain/drizzle within the boundary layer. Different types of scatter targets (from the boundary layer particles, through rain, drizzle, supercooled layer, ice cloud, liquid cloud, aerosol, to molecules) are classified using the synergy of lidar, cloud radar, and microwave radiometer, so that our work fits very well within the core tasks of the European Cooperation in Science and Technology (COST) Action for the Profiling of the atmospheric Boundary layer on a European scale (PROBE) [78].

Funding

European Cooperation in Science and Technology (PROBE, CA18235); European Space Agency (POLIMOS 4000119961/16/NL/FF/mg, RAMOS 4000118115/16/NL/FF/gp); Narodowe Centrum Nauki (Preludium-15 UMO-2018/29/N/ST10/02628); National Key Research and Development Program of China (2018YFC0213101, 2016YFC1400905).

Acknowledgments

We acknowledge Bogdan Chojnicki, the PI of the PolWET site, for granting an access to the experimental site of the Poznan University of Life Sciences (PULS). Patryk Poczta (PULS) for conducting lidar measurement. Damian Józwiak (PULS), Rafal Fortuna (University of Warsaw, UW), George Georgoussis, Alex Louridas and Christos Evangelatos (Raymetrics, Greece), Bernhard Stein and Bernd Mielke (LiCEL GmbH, Germany), Matthias Resch (Innolas Laser GmbH, Germany) and Georgios Tzeremes (ESA-ESTEC, The Netherlands), for their technical support. The EMORAL lidar is a property of the European Space Agency (ESA). It was developed by Raymetrics in a collaborative R&D effort with the University of Warsaw (UW), the Ludwig-Maximilians-Universität München (LMU), the National Observatory of Athens (NOA), and the European Space Agency (ESA). The BASTA cloud radar was developed by the Laboratoire Atmosphères, Milieux, Observations Spatiales (LATMOS). The HATPRO-G2

microwave radiometer (Radiometer Physics GmbH, Germany) is a property of the Romanian National Institute of R&D for Optoelectronics (INOE).

D.W. and I.S.S. wrote the paper, designed the study concept, conducted formal analyses, made an extensive literature review, and holistically interpreted the results. D.W. coded all algorithms and performed sensitivity tests to assess their performance. I.S.S. and D.S. contributed to the lidar development, setting up and conducting the experiment, as well as taking care of the quality assurance of lidar data. J.D. contributed with the cloud radar system development, the target classification for cloud radar, and its data interpretation. D.E. provided the microwave radiometer and contributed with the interpretation of its data. I.S.S. and X.S. developed a synergetic algorithm for target classification and contributed to the assessment of classification quality. I.S.S., D.W., D.E. and X.S. obtained funding to conduct the research. All authors contributed to the interpretation and discussion of the results and conducted revisions of the paper.

Disclosures

The authors declare no conflict of interest.

References

1. M. D. Fielding, J. C. Chiu, R. J. Hogan, G. Feingold, E. Eloranta, E. J. O'Connor, and M. P. Cadeddu, "Joint retrievals of cloud and drizzle in marine boundary layer clouds using ground-based radar, lidar and zenith radiances," *Atmos. Meas. Tech.* **8**(7), 2663–2683 (2015).
2. K. Sarna and H. W. J. Russchenberg, "Ground-based remote sensing scheme for monitoring aerosol–cloud interactions," *Atmos. Meas. Tech.* **9**(3), 1039–1050 (2016).
3. H. Baars, T. Kanitz, R. Engelmann, D. Althausen, B. Heese, M. Komppula, J. Preißler, M. Tesche, A. Ansmann, U. Wandinger, J. H. Lim, J. Y. Ahn, I. S. Stachlewska, V. Amiridis, E. Marinou, P. Seifert, J. Hofer, A. Skupin, F. Schneider, S. Bohlmann, A. Foth, S. Bley, A. Pfüller, E. Giannakaki, H. Lihavainen, Y. Viisanen, R. K. Hooda, S. N. Pereira, D. Bortoli, F. Wagner, I. Mattis, L. Janicka, K. M. Markowicz, P. Achtert, P. Artaxo, T. Pauliquevis, R. A. F. Souza, V. P. Sharma, P. G. van Zyl, J. P. Beukes, J. Sun, E. G. Rohwer, R. Deng, R. E. Mamouri, and F. Zamorano, "An overview of the first decade of PollyNET: an emerging network of automated Raman-polarization lidars for continuous aerosol profiling," *Atmos. Chem. Phys.* **16**(8), 5111–5137 (2016).
4. E. Marinou, M. Tesche, A. Nenes, A. Ansmann, J. Schrod, D. Mamali, A. Tsekeri, M. Pikridas, H. Baars, R. Engelmann, K. A. Voudouri, S. Solomos, J. Sciare, S. Groß, F. Ewald, and V. Amiridis, "Retrieval of ice-nucleating particle concentrations from lidar observations and comparison with UAV in situ measurements," *Atmos. Chem. Phys.* **19**(17), 11315–11342 (2019).
5. J. H. Seinfeld, C. Bretherton, K. S. Carslaw, H. Coe, P. J. DeMott, E. J. Dunlea, G. Feingold, S. Ghan, A. B. Guenther, R. Kahn, and I. Kraucunas, "Improving our fundamental understanding of the role of aerosol–cloud interactions in the climate system," *Proc. Natl. Acad. Sci. U. S. A.* **113**(21), 5781–5790 (2016).
6. K. Markowicz, M. T. Chilinski, J. Lisok, O. Zawadzka, I. S. Stachlewska, L. Janicka, A. Rozwadowska, P. Makuch, P. Pakszys, T. Zielinski, T. Petelski, M. Posyniak, A. Pietruczuk, A. Szkop, and D. L. Westphal, "Study of aerosol optical properties during long-range transport of biomass burning from Canada to Central Europe in July 2013," *J. Aeros. Sci.* **101**, 156–173 (2016).
7. Z. Li, F. Niu, J. Fan, Y. Liu, D. Rosenfeld, and Y. Ding, "Long-term impacts of aerosol on the vertical development of clouds and precipitation," *Nat. Geosci.* **4**(12), 888–894 (2011).
8. P. Hasekamp, "Capability of multi-viewing-angle photo-polarimetric measurements for the simultaneous retrieval of aerosol and cloud properties," *Atmos. Meas. Tech.* **3**(4), 839–851 (2010).
9. M. Ceccaldi, J. Delanoë, R. J. Hogan, N. L. Pounder, A. Protat, and J. Pelon, "From CloudSat–CALIPSO to EarthCare: Evolution of the DARDAR cloud classification and its comparison to airborne radar–lidar observations," *J. Geophys. Res.* **118**(14), 7962–7981 (2013).
10. J. Delanoë and R. J. Hogan, "A variational scheme for retrieving ice cloud properties from combined radar, lidar and infrared radiometer," *J. Geophys. Res.* **113**(D7), D07204 (2008).
11. H. Pawlowska and J.L. Brenguier, "Microphysical properties of stratocumulus clouds during ACE–2," *Tellus B* **52**(2), 868–887 (2000).
12. J. Delanoë and R. J. Hogan, "Combined CloudSat–CALIPSO–MODIS retrievals of the properties of ice clouds," *J. Geophys. Res.* **115**, D00H29 (2010).
13. J. L. Brenguier, H. Pawlowska, and L. Schüller, "Cloud microphysical and radiative properties for parameterization and satellite monitoring of the indirect effect of aerosol on climate," *J. Geophys. Res.* **108**(D15), 8632 (2003).
14. E. Gryspeerd, O. Sourdeval, J. Quaas, J. Delanoë, M. Krämer, and P. Kühne, "Ice crystal number concentration estimates from lidar–radar satellite remote sensing – Part 2: Controls on the ice crystal number concentration," *Atmos. Chem. Phys.* **18**(19), 14351–14370 (2018).

15. C. Listowski, J. Delanoë, A. Kirchgaessner, T. Lachlan-Cope, and J. King, "Antarctic clouds, supercooled liquid water and mixed phase, investigated with DARDAR: geographical and seasonal variations," *Atmos. Chem. Phys.* **19**(10), 6771–6808 (2019).
16. G. L. Stephens, D. G. Vane, R. J. Boain, G. G. Mace, K. Sassen, Z. Wang, A. J. Illingworth, E. J. O'Connor, W. B. Rossow, S. L. Durden, S. D. Miller, R. T. Austin, A. Benedetti, C. Mitrescu, and T. C. S. Team, "The Cloudsat mission and the A-train: A new dimension of space-based observations of clouds and precipitation," *B. Am. Meteorol. Soc.* **83**(12), 1771–1790 (2002).
17. Z. B. Zhang, A. S. Ackerman, G. Feingold, S. Platnick, R. Pincus, and H. W. Xue, "Effects of cloud horizontal inhomogeneity and drizzle on remote sensing of cloud droplet effective radius: case studies based on large-eddy simulations," *J. Geophys. Res.* **117**(D19), D19208 (2012).
18. J. Illingworth, R. J. Hogan, E. J. O'Connor, D. Bouniol, M. E. Brooks, J. Delanoë, D. P. Donovan, J. D. Eastment, N. Gaussiat, J. W. F. Goddard, M. Haefelin, H. K. Baltink, O. A. Krasnov, J. Pelon, J. M. Piriou, A. Protat, H. W. J. Russchenberg, A. Seifert, A. M. Tompkins, G. J. van Zadelhoff, F. Vinit, U. Willen, and D. R. Wilson, and C. L. Wrench, "Cloudnet – continuous evaluation of cloud profiles in seven operational models using ground-based observations," *B. Am. Meteorol. Soc.* **88**(6), 883–898 (2007).
19. D. Zhang, Z. Wang, and D. Liu, "A global view of midlevel liquid-layer topped stratiform cloud distribution and phase partition from CALIPSO and CloudSat measurements," *J. Geophys. Res.* **115**, D00K30 (2010).
20. E. J. O'Connor, R. J. Hogan, and A. J. Illingworth, "Retrieving Stratocumulus Drizzle Parameters Using Doppler Radar and Lidar," *J. Appl. Meteorol.* **44**(1), 14–27 (2005).
21. M. J. McGill, D. Hlavka, W. Hart, V. S. Scott, J. Spinhirne, and B. Schmid, "Cloud physics lidar: Instrument description and initial measurement results," *Appl. Opt.* **41**(18), 3725–3734 (2002).
22. H. Omar, D. M. Winker, C. Kittaka, M. A. Vaughan, Z. Liu, Y. Hu, C. R. Trepte, R. R. Rogers, R. A. Ferrare, K. P. Lee, R. E. Kuehn, and C. A. Hostetler, "The CALIPSO automated aerosol classification and lidar ratio selection algorithm," *J. Atmos. Oceanic Technol.* **26**(10), 1994–2014 (2009).
23. J. Delanoë, A. Protat, O. Jourdan, J. Pelon, M. Papazzoni, R. Dupuy, J. F. Gayet, and C. Jouan, "Comparison of airborne in situ, airborne radar-lidar, and spaceborne radar-lidar retrievals of polar ice cloud properties sampled during the POLARCAT campaign," *J. Atmos. Oceanic Technol.* **30**(1), 57–73 (2013).
24. H. Baars, P. Seifert, R. Engelmann, and U. Wandinger, "Target categorization of aerosol and clouds by continuous multiwavelength-polarization lidar measurements," *Atmos. Meas. Tech.* **10**(9), 3175–3201 (2017).
25. F. Immler, R. Treffeisen, D. Engelbart, K. Kruger, and O. Schrems, "Cirrus, contrails, and ice supersaturated regions in high pressure systems at northern mid latitudes," *Atmos. Chem. Phys.* **8**(6), 1689–1699 (2008).
26. I. S. Stachlewska and C. Ritter, "On retrieval of lidar extinction profiles using Two-Stream and Raman techniques," *Atmos. Chem. Phys.* **10**(6), 2813–2824 (2010).
27. Z. Wang and K. Sassen, "Cirrus cloud microphysical property retrieval using lidar and radar measurements. Part I: Algorithm description and comparison with in situ data," *J. Appl. Meteorol.* **41**(3), 218–229 (2002).
28. C. Mätzler, P. W. Rosenkranz, and J. Cermak, "Microwave absorption measurements of supercooled clouds and implications for the dielectric properties of water," IAP Res. Rep. 2010-02-MW, Institute for Applied Physics, University of Bern, Bern, Switzerland. 2010.
29. C. Mätzler, P. W. Rosenkranz, and J. Cermak, "Microwave absorption of supercooled clouds and implications for the dielectric properties of water," *J. Geophys. Res.* **115**(D23), D23208 (2010).
30. Z. Sokol, J. Minářová, and P. Novák, "Classification of Hydrometeors Using Measurements of the Ka-Band Cloud Radar Installed at the Milešovka Mountain (Central Europe)," *Remote Sens.* **10**(11), 1674 (2018).
31. S. K. Das, M. Konwar, K. Chakravarty, and S. M. Deshpande, "Raindrop size distribution of different cloud types over the Western Ghats using simultaneous measurements from micro-rain radar and disdrometer," *Atmos. Res.* **186**, 72–82 (2017).
32. D. Nicolae, J. Vasilescu, C. Talianu, I. Biniotoglou, V. Nicolae, S. Andrei, and B. Antonescu, "A neural network aerosol-typing algorithm based on lidar data," *Atmos. Chem. Phys.* **18**(19), 14511–14537 (2018).
33. Z. Wang and K. Sassen, "Cloud type and macrophysical property retrieval using multiple remote sensors," *J. Appl. Meteorol.* **40**(10), 1665–1682 (2001).
34. J. Heymsfield, A. Protat, D. Bouniol, R. T. Austin, R. J. Hogan, J. Delanoë, H. Okamoto, K. Sato, G. J. van Zadelhoff, D. P. Donovan, and Z. Wang, "Testing IWC retrieval methods using radar and ancillary measurements with in situ data," *J. Appl. Meteorol. Climatol.* **47**(1), 135–163 (2008).
35. D. Bouniol, A. Protat, J. Delanoë, J. Pelon, J. M. Piriou, F. Bouysse, A. Tompkins, D. R. Wilson, Y. Morille, M. Haefelin, E. J. O'Connor, R. Hogan, A. J. Illingworth, D. P. Donovan, and H. K. Baltink, "Using continuous ground-based radar and lidar measurements for evaluating the representation of clouds in four operational models," *J. Appl. Meteorol. Climatol.* **49**(9), 1971–1991 (2010).
36. I. S. Stachlewska, M. Costa-Surós, and D. Althausen, "Raman lidar water vapour profiling over Warsaw, Poland," *Atmos. Res.* **194**, 258–267 (2017).
37. D. Wang, I. S. Stachlewska, X. Song, B. Heese, and A. Nemuc, "Variability of boundary layer over an urban continental site based on 10 years of active remote sensing observations in Warsaw," *Remote Sens.* **12**(2), 340 (2020).
38. I. S. Stachlewska, O. Zawadzka, and R. Engelmann, "Effect of heat wave conditions on aerosol optical properties derived from satellite and ground-based remote sensing over Poland," *Remote Sens.* **9**(11), 1199 (2017).

39. I. S. Stachlewska, M. Samson, O. Zawadzka, K. M. Harenda, L. Janicka, P. Poczta, D. Szczepanik, B. Heese, D. Wang, K. Borek, E. Tetoni, E. Proestakis, N. Siomos, A. Nemuc, B. H. Chojnicki, K. M. Markowicz, A. Pietruczuk, A. Szkop, D. Althausen, K. Stebel, D. Schuettemeyer, and C. Zehner, "Modification of Local Urban Aerosol Properties by Long-Range Transport of Biomass Burning Aerosol," *Remote Sens.* **10**(3), 412 (2018).
40. D. Wang, D. Szczepanik, and I. S. Stachlewska, "Interrelations between surface, boundary layer, and columnar aerosol properties derived in summer and early autumn over a continental urban site in Warsaw, Poland," *Atmos. Chem. Phys.* **19**(20), 13097–13128 (2019).
41. L. Janicka, I. S. Stachlewska, I. Veselovskii, and H. Baars, "Temporal variations in optical and microphysical properties of mineral dust and biomass burning aerosol derived from daytime Raman lidar observations over Warsaw, Poland," *Atmos. Environ.* **169**, 162–174 (2017).
42. V. Freudenthaler, H. Linné, A. Chaikovski, D. Rabus, and S. and Groß, "EARLINET lidar quality assurance tools," *Atmos. Meas. Tech. Discuss.*, in review, 2018.
43. C. Böckmann, U. Wandinger, A. Ansmann, J. Bösenberg, V. Amiridis, A. Boselli, A. Delaval, F. De Tomasi, M. Frioud, and I. V. Grigorov, "Aerosol lidar intercomparison in the framework of the EARLINET project. 2. Aerosol backscatter algorithms," *Appl. Opt.* **43**(4), 977–989 (2004).
44. G. Pappalardo, A. Amodeo, A. Apituley, A. Comeron, V. Freudenthaler, H. Linné, A. Ansmann, J. Bösenberg, G. D'Amico, I. Mattis, L. Mona, U. Wandinger, V. Amiridis, L. AladosArboledas, D. Nicolae, and M. Wiegner, "EARLINET: towards an advanced sustainable European aerosol lidar network towards an advanced sustainable European aerosol lidar network," *Atmos. Meas. Tech.* **7**(8), 2389–2409 (2014).
45. J. Delanoë, A. Protat, J. P. Vinson, W. Brett, C. Caudoux, F. Bertrand, J. Parent du Chatelet, R. Hallali, L. Barthes, M. Haefelin, and J. C. Dupont, "BASTA: A 95-GHz FMCW Doppler radar for cloud and fog studies," *J. Atmos. Oceanic Technol.* **33**(5), 1023–1038 (2016).
46. R. J. Hogan, D. Bouniol, D. N. Ladd, E. J. O'Connor, and A. J. Illingworth, "Absolute calibration of 94/95-GHz radars using rain," *J. Atmos. Oceanic Technol.* **20**(4), 572–580 (2003).
47. F. Toledo, J. Delanoë, M. Haefelin, and J.-C. Dupont, "Absolute Calibration method for FMCW Cloud Radars," *Atmos. Meas. Tech. Discuss.*, in review, 2020.
48. K. Fragkos, B. Antonescu, D. M. Giles, D. Ene, M. Boldeanu, G. A. Efsthathiou, L. Belegante, and D. Nicolae, "Assessment of the total precipitable water from a sun photometer, microwave radiometer and radiosondes at a continental site in southeastern Europe," *Atmos. Meas. Tech.* **12**(3), 1979–1997 (2019).
49. T. Rose, S. Crewell, U. Löhnert, and C. Simmer, "A network suitable microwave radiometer for operational monitoring of the cloudy atmosphere," *Atmos. Res.* **75**(3), 183–200 (2005).
50. L. D. Labzovskii, A. Papayannis, I. Biniotoglou, R. F. Banks, J. M. Baldasano, F. Toanca, C. G. Tzanis, and J. Christodoulakis, "Relative humidity vertical profiling using lidar-based synergistic methods in the framework of the Hygra-CD campaign," *Ann. Geophys.* **36**(1), 213–229 (2018).
51. L. Liljegren, "Microwave Radiometer Profiles Handbook, Manual," Argonne National Laboratory, Washington D.C., 2002.
52. H. M. Cho, P. Yang, G. W. Kattawar, S. L. Nasiri, Y. Hu, P. Minnis, C. Trepte, and D. Winker, "Depolarization ratio and attenuated backscatter for nine cloud types: analyses based on collocated CALIPSO lidar and MODIS measurements," *Opt. Express* **16**(6), 3931–3948 (2008).
53. J. D. Klett, "Stable analytical inversion solution for processing lidar returns," *Appl. Opt.* **20**(2), 211–220 (1981).
54. G. Fernald, "Analysis of atmospheric lidar observations – some comments," *Appl. Opt.* **23**(5), 652–653 (1984).
55. V. Freudenthaler, M. Esselborn, M. Wiegner, B. Heese, M. Tesche, A. Ansmann, D. Müller, D. Althausen, M. Wirth, A. Fix, G. Ehret, P. Knippertz, C. Toledano, J. Gasteiger, M. Garhammer, and M. Seefeldner, "Depolarization ratio profiling at several wavelengths in pure Saharan dust during SAMUM 2006," *Tellus B* **61**(1), 165–179 (2009).
56. V. Freudenthaler, "About the effects of polarising optics on lidar signals and the $\Delta 90$ calibration," *Atmos. Meas. Tech.* **9**(9), 4181–4255 (2016).
57. K. Sassen, "Polarization in Lidar," *Lidar*, C. Weitkam, eds., Springer Press: New York. 19–42 (2005).
58. A. Ansmann, P. Seifert, M. Tesche, and U. Wandinger, "Profiling of fine and coarse particle mass: case studies of Saharan dust and Eyjafjallajökull/Grimsvötn volcanic plumes," *Atmos. Chem. Phys.* **12**(20), 9399–9415 (2012).
59. Z. Liu, M. Vaughan, D. Winker, C. Kittaka, B. Getzewich, R. Kuehn, A. Omar, K. Powell, C. Trepte, and C. Hostetler, "The CALIPSO lidar cloud and aerosol discrimination: Version 2 algorithm and initial assessment of performance," *J. Atmos. Oceanic Technol.* **26**(7), 1198–1213 (2009).
60. S. P. Burton, R. A. Ferrare, C. A. Hostetler, J. W. Hair, R. R. Rogers, M. D. Obland, C. F. Butler, A. L. Cook, D. B. Harper, and K. D. Froyd, "Aerosol classification using airborne High Spectral Resolution Lidar measurements – methodology and examples," *Atmos. Meas. Tech.* **5**(1), 73–98 (2012).
61. D. M. Winker, M. A. Vaughan, A. Omar, Y. Hu, K. A. Powell, Z. Liu, W. H. Hunt, and S. A. Young, "Overview of the CALIPSO mission and CALIOP data processing algorithms," *J. Atmos. Ocean. Tech* **26**(11), 2310–2323 (2009).
62. J. P. Vernier, T. D. Fairlie, M. Natarajan, F. G. Wienhold, J. Bian, B. G. Martinsson, S. Crumeyrolle, L. W. Thomason, and K. M. Bedka, "Increase in upper tropospheric and lower stratospheric aerosol levels and its potential connection with Asian pollution," *J. Geophys. Res.* **120**(4), 1608–1619 (2015).
63. S. P. Burton, J. W. Hair, M. Kahnert, R. A. Ferrare, C. A. Hostetler, A. L. Cook, D. B. Harper, T. A. Berkoff, S. T. Seaman, J. E. Collins, M. A. Fenn, and R. R. Rogers, "Observations of the spectral dependence of linear particle

- depolarization ratio of aerosol using NASA Langley airborne High Spectral Resolution Lidar,” *Atmos. Chem. Phys.* **15**(23), 13453–13473 (2015).
64. V. V. Zuev, V. D. Burlakov, A. V. Nevzorov, V. L. Pravdin, E. S. Savelieva, and V. V. Gerasimov, “30-year lidar observations of the stratospheric aerosol layer state over Tomsk (Western Siberia, Russia),” *Atmos. Chem. Phys.* **17**(4), 3067–3081 (2017).
 65. K. Srivastava, P. Pant, P. Hegde, S. Singh, U. C. Dumka, M. Naja, N. Singh, and Y. Bhavanikumar, “The Influence of a South Asian Dust Storm on Aerosol Radiative Forcing at a High-Altitude Station in Central Himalayas,” *Int. J. Remote. Sens.* **32**(22), 7827–7845 (2011).
 66. A. Dörnbrack, I. S. Stachlewska, C. Ritter, and R. Neuber, “Aerosol distribution around Svalbard during intense easterly winds,” *Atmos. Chem. Phys.* **10**(4), 1473–1490 (2010).
 67. S. Groß, M. Esselborn, B. Weinzierl, M. Wirth, A. Fix, and A. Petzold, “Aerosol classification by airborne high spectral resolution lidar observations,” *Atmos. Chem. Phys.* **13**(5), 2487–2505 (2013).
 68. S. P. Burton, M. A. Vaughan, R. A. Ferrare, and C. A. Hostetler, “Separating mixtures of aerosol types in airborne High Spectral Resolution Lidar data,” *Atmos. Meas. Tech.* **7**(2), 419–436 (2014).
 69. A. Borovoi, Y. Balin, G. Kokhanenko, I. Penner, A. Konoshonkin, and N. Kustova, “Layers of quasi-horizontally oriented ice crystals in cirrus clouds observed by a two-wavelength polarization lidar,” *Opt. Express* **22**(20), 24566–24573 (2014).
 70. A. Nemuc, J. Vasilescu, C. Talianu, L. Belegante, and D. Nicolae, “Assessment of aerosol’s mass concentrations from measured linear particle depolarization ratio (vertically resolved) and simulations,” *Atmos. Meas. Tech.* **6**(11), 3243–3255 (2013).
 71. D. Müller, A. Ansmann, I. Mattis, M. Tesche, U. Wandinger, D. Althausen, and G. Pisani, “Aerosol-type-dependent lidar ratios observed with Raman lidar,” *J. Geophys. Res.* **112**(D16), D16202 (2007).
 72. B. Heese and M. Wiegner, “Vertical aerosol profiles from Raman polarization lidar observations during the dry season AMMA field campaign,” *J. Geophys. Res.* **113**, D00C11 (2008).
 73. C. Córdoba-Jabonero, M. Sicard, A. Ansmann, A. del Águila, and H. Baars, “Separation of the optical and mass features of particle components in different aerosol mixtures by using POLIPHON retrievals in synergy with continuous polarized Micro-Pulse Lidar (P-MPL) measurements,” *Atmos. Meas. Tech.* **11**(8), 4775–4795 (2018).
 74. A. Ansmann, M. Tesche, P. Knippertz, E. Bierwirth, D. Althausen, D. Mueller, and O. Schulz, “Vertical profiling of convective dust plumes in Southern Morocco during SAMUM,” *Tellus B* **61**(1), 340–353 (2009).
 75. R. J. Hogan and E. J. O’Connor, “Facilitating cloud radar and lidar algorithms: The Cloudnet Instrument Synergy/Target Categorization product,” Cloudnet documentation. 2004.
 76. A. Reehorst, D. Brinker, M. Politovich, D. Serke, C. Ryerson, A. Pazmany, and F. Solheim, “Progress towards the remote sensing of aircraft icing hazards, in Remote Sensing Applications for Aviation Weather Hazard Detection and Decision Support,” *Proc. SPIE* **7088**, 70880J (2008).
 77. R. J. Hogan, M. D. Behera, E. J. O’Connor, and A. J. Illingworth, “Estimate of the global distribution of stratiform supercooled liquid water clouds using the lite lidar,” *Geophys. Res. Lett.* **31**(5), L05106 (2004).
 78. D. Cimini, M. Haeffelin, S. Kotthaus, U. Löhnert, P. Martinet, E. O’Connor, C. Walden, M. Collaud Coen, and J. Preissler, “Towards the profiling of the atmospheric boundary layer at European scale – Introducing the COST Action PROBE,” *B. Atmos. Sci. Tech.* **1**(1), 1–11 (2020).